Probing Spin Wave Diffraction Patterns of Curved Antennas

L. Temdie,[1,†] V. Castel,[1,†] M.B. Jungfleisch,[2] R. Bernard,[3] H. Majjad,[3]
D. Stoeffler,[3] Y. Henry,[3] M. Bailleul,[3] and V. Vlaminck[1,*,†]

[1] *IMT Atlantique, Department MO, Lab-STICC—UMR 6285 CNRS, Technopole Brest-Iroise CS83818, Brest Cedex 03, 29238 France*
[2] *Department of Physics and Astronomy, University of Delaware, Newark, Delaware, USA*
[3] *Université de Strasbourg, CNRS, Institut de Physique et Chimie des Matériaux de Strasbourg, UMR 7504, Strasbourg F-67000, France*

(Received 12 September 2023; revised 7 November 2023; accepted 22 December 2023; published 18 January 2024; corrected 3 June 2024)

We report on the dependence of curvilinear-shaped coplanar waveguides on the near-field diffraction (NFD) patterns of spin waves propagating in perpendicularly magnetized thin films. Implementing the propagating spin-wave spectroscopy techniques on either concentrically or eccentrically shaped antennas, we show how the link budget is directly affected by the spin-wave interference, in good agreement with NFD simulations. This work demonstrates the feasibility of inductively probing a magnon interference pattern with a resolution down to 1 μm^2, and provides a methodology for shaping spin-wave beams from an antenna design. This methodology is successfully implemented in the case study of a spin-wave Young's interference experiment.

DOI: 10.1103/PhysRevApplied.21.014032

I. INTRODUCTION

The collective excitations of a spin ensemble, known as spin waves (or magnons for their quanta) [1], are the subject of substantial interest as potential information carriers for unconventional electronic applications [2–5]. The versatility of the magnon dispersion in the broad microwave range offers a vast field of exploration for the development of wave-based computing technologies [6–8], in which information could be encoded in both the phase and the amplitude of the spin wave. The various nonlinear mechanisms, along with their nanoscale integrability, [9] make this a system of choice for the development of novel architectures such as neuromorphic computing [10,11], reservoir computing [12,13], holographic memory [14,15], and spectral analysis [16], which are all interference-based techniques. Furthermore, the wide variety of nonreciprocal effects inherent in spin dynamics [17–22] generates considerable interest in reducing the dimensions of analog signal processing components such as microwave isolators, circulators, filters, directional couplers, and phase shifters.

Basic concepts of optics applied to spin waves recently revealed the possibility of shaping and steering spin-wave beams at the submicrometer scale [23–26], opening up new perspectives for the development of interferometric magnonic devices. Alongside these efforts, we developed a robust model to map the near-field diffraction (NFD) pattern of arbitrary shaped antennas [27], which allows one to comprehend the magnon beamforming in extended thin films as a result of the excitation geometry.

In this article, we experimentally probe via out-of-plane spin-wave spectroscopy the diffraction pattern of curvilinear antennas. The paper is organized as follows. In Sec. II, we present a comparative study of spin-wave transduction between straight and concentric pairs of coplanar waveguides (CPWs). In Sec. III, we study an antenna geometry that is akin to a Young's interference experiment for spin waves. The design of these experiments relies on an NFD simulation [27], which was proven to benchmark spin-wave diffraction in thin films for arbitrary excitation geometries.

II. CONCENTRIC VERSUS STRAIGHT ANTENNAS

A. Sample fabrication and measurement protocol

We first compare the transduction of spin waves between pairs of identical straight antennas with that of quarter-circular concentric antennas, for which we kept the same separation distance D, and the same length of excitation antenna, $L_{ant} = (\pi/2)R \approx 15.7\ \mu m$ ($R = 10\ \mu m$). Figures 2(a) and 2(b) show scanning electron microscope (SEM)

*vincent.vlaminck@imt-atlantique.fr
†Also at Lab-STICC—UMR 6285 CNRS, Technopole Brest-Iroise CS83818, 29238 Brest Cedex 03.

images of two such antennas devices with a separation distance of $D = 8$ μm, which consist of a gold CPW with the following dimensions: a central line of $S = 400$ nm width, and ground lines of $G = 200$ nm width, spaced by 200 nm. These CPW dimensions produce a wave packet centered around $k_1 = 5.92$ rad μm^{-1} [27]. The antennas were fabricated on top of an extended 30-nm-thin sputtered yttrium iron garnet (YIG) film [28] via electron beam lithography, followed by liftoff of 5 nm Ti/60 nm Au. A 40-nm SiO_2 spacer was deposited on top of the YIG film prior to the process. For this study, we also fabricated similar comparative devices with a separation distance of $D = 5$ μm.

The sample is placed directly onto the pole of a vertical electromagnet that can reach up to 1.3 T at 5 A, and contacted via 150 μm-pitch picoprobe to an Agilent E8342B-50GHz vector network analyzer. We proceed to spin-wave spectroscopy measurement at constant applied field sweeping the frequency in the 1–12-GHz range. In order to resolve a zero base line, we always subtract reference spectra acquired at different applied values (H_{ref}), for which no resonant feature occurs within the frequency sweep. Furthermore, we convert the S_{ij} matrix to the impedance matrix Z_{ij}, which we divide by $i\omega$ to represent our spectra in units of inductance, in accordance with the inductive nature of the coupling between a spin wave and a CPW [29,30],

$$\Delta L_{ab}(f, H) = \frac{1}{i\omega}(Z_{ab}(f, H) - Z_{ab}(f, H_{\text{ref}})), \quad (1)$$

where the subscripts a, b denote either a transmission measurement from port b to port a, or a reflection measurement done on the same port if $a = b$.

B. Spin-wave spectroscopy

Figures 1(c) and 1(d) shows reflection (blue) and transmission (red) spectra obtained at 279 mT and 465 mT and an input power of −15 dBm, respectively, for a pair of straight antennas (upper panel), and for a pair of concentric antennas (lower panel), both with a separation distance of 8 μm. We identify two main peaks from the reflection spectra. The first peak has a larger amplitude and appears at lower frequency. It corresponds to the ferromagnetic resonance peak ($k \approx 0$), namely, the region of the CPW extending from the 150- μm-pitch picoprobe contacts to the slightly reduced section of the CPW, yet wider than 10 μm. The second peak corresponds to the k_1 submicrometer termination of the CPW shown in Figs. 1(a) and 1(b), where microwave power is transmitted from port 1 to port 2 via spin waves. One notices in particular the seeming lack of reflection peak ΔL_{22} for the 2- μm-radius circular probe antenna [Fig. 1(d)], in accordance with the proportionality of the signal amplitude with the length of the antenna. In a self-inductive spin-wave detection, the signal amplitude scales with the aspect ratio length over the width of the antenna. In the case of the pair of concentric antennas separated by 8 μm, there is an antenna length ratio between antenna 1 and antenna 2 of about 5 (e.g.,

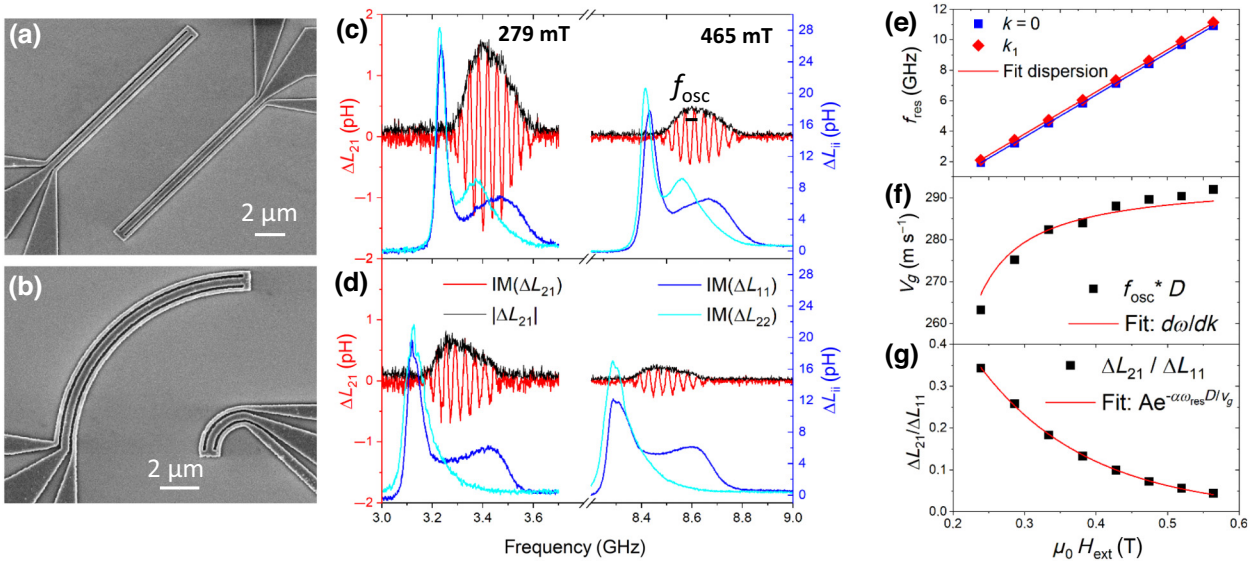

FIG. 1. (a) Scanning electron microscope (SEM) image of a pair of identical straight antennas. (b) SEM image of a concentric antenna device. Propagating spin-wave spectra measured at 279 mT and 465 mT, respectively, for straight antennas (c), and concentric antennas (d). Magnetic characterization done on the straight antenna device. Field dependence of: (e) the resonance frequency of both $k \approx 0$ and $k_1 = 5.92$ rad μm^{-1} modes, (f) the measured group velocity fitted with the derivative of the dispersion relation, (g) the measured spectra amplitude fitted with an exponential decay, for which we adopted the low wave-vector approximation of the attenuation length $L_{\text{att}} = v_g/2\pi\alpha f_{\text{res}}$.

R_1/R_2), which is comparable with the ratio of amplitude between ΔL_{11} and ΔL_{22}.

The transmission spectra reveal the typical features of propagating spin-wave spectra [25,30], namely oscillations convoluted with an envelope, that is, the black and red lines in Figs. 2(b) and 2(c), respectively. The oscillatory signature of the transmission spectra is due to the nature of the excitation, which is not purely monochromatic. Assuming that the group velocity remains fairly constant within the wave-vector range for a single peak, two wave vectors k_1 and k_2 resonating respectively at f_1 and f_2, will accumulate a phase difference over a propagation distance D of $\delta\phi = |k_1 - k_2|D \approx 2\pi|f_2 - f_1| \cdot D/v_g$. For a complete oscillation (e.g., when $\delta\phi = 2\pi$), which we denote by f_{osc}, it gives the relation $v_g = f_{\text{osc}}D$. Besides, one notices that the envelope appears less symmetrical with respect to frequency for the concentric geometry than for the straight one, which is likely due to interferences caused by the NFD pattern of the concentric antenna.

More importantly, we observe a clear diminution of amplitude for the concentric geometry compared with the straight one, with a rather constant ratio $\Delta L_{21}^{\text{concentric}}/\Delta L_{21}^{\text{straight}} \approx 0.43$ over the whole frequency range. This observation may seem surprising at first, considering the confined nature of the radiation pattern with respect to the probe antenna definition [cf. Fig. 2(b)], and knowing that we kept the same length of antenna for the excitation, and the same separation distance for both geometries. Spin-wave dispersion in out-of-plane magnetized films is known to be isotropic, and considering that an equal amount of power radiates inwards or outwards from the circular antennas, one might expect a comparable amplitude between straight and concentric geometries.

However, one can grasp this difference of amplitude by making an analogy with the Friis transmission formula used in telecommunications engineering [31], which relates received and emitted powers between two radio antennas to the product of their effective aperture area, in accordance with the concept of directivity for an antenna having uniform and equiphase aperture. In our case, the spin-wave propagates in a two-dimensional plane, therefore, we assimilate the aperture to the length $l_{1,2}$ of the spin-wave antennas (e.g., $l_{1,2} = (\pi/2)R_{1,2}$). Also, the transmission spectra ΔL_{21} are obtained from the measurement of S_{21} parameters, which corresponds to a ratio of wave amplitude, and therefore relates to the square root of the power. For these reasons, the adaptation of the Friis formula for a spin-wave transduction between two antennas should result in $\Delta L_{21} \propto \sqrt{l_1 l_2/D\lambda}$, and therefore, the amplitude ratio between concentric and straight geometries should be proportional to the square root of the ratio of the arc lengths: $\Delta L_{21}^{\text{concentric}}/\Delta L_{21}^{\text{straight}} = \sqrt{R_2/R_1} = 0.45$. Still, this agreement should be viewed cautiously as the Friis formula is normally applicable in the far-field region to ensure a plane wave front at the receiving antenna, which corresponds here to a propagation distance $D \geq (\pi R_1)^2/\lambda \approx 1$ mm. For this reason, we ought to resort to NFD simulations in order to assess the conformity of our measurements.

Figures 1(e)–1(g) present the methodology used to evaluate the magnetic properties used in the NFD simulations, from the spin-wave spectroscopy performed over the whole field range on a single pair of straight antenna, for which we can ensure a plane wave profile. Firstly, we track the field dependence of the $k = 0$ reflection peak and the transmission peak as shown in Fig. 1(e), and fit it to the magnetostatic forward volume waves (MSFVW) dispersion relation [32,33], which gives a gyromagnetic ratio $\gamma/2\pi = 28.2 \pm 0.1$ GHz $\cdot$ T^{-1}, an effective magnetization $\mu_0 M_s = 185 \pm 5$ mT more or less equal to the saturation magnetization, suggesting no uniaxial anisotropy for our YIG film. We then estimate the group velocities v_g from the period of oscillation of the transmission spectra

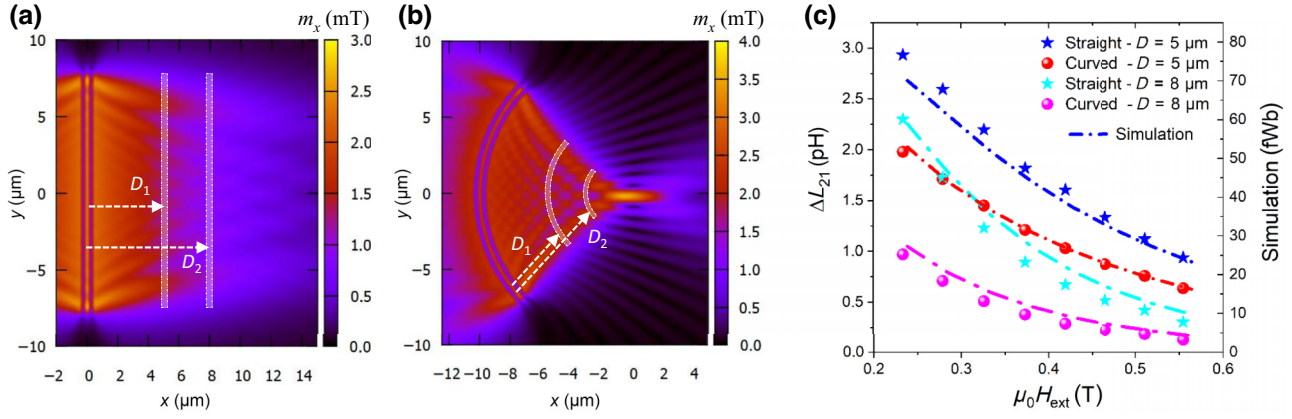

FIG. 2. Near-field diffraction simulations at $\mu_0 H_{\text{ext}} = 419.2$ mT, $f_{\text{exc}} = 6.892$ GHz for (a) a 15.7-μm-long straight antenna, and (b) 10 μm-radius quarter-circular antenna. The white areas represent regions sensed by the detection antenna located at distance of $D_1 = 5$ μm or $D_2 = 8$ μm from the excitation antenna. (c) Comparison of the straight and concentric spin-wave amplitude with the emulated inductive signal from the near-field diffraction simulations.

[25,30], and fit its field dependence to the dispersion relation as shown in Fig. 1(f), letting only the exchange constant as a free parameter, which gives $A_{\text{exch}} = 3.5 \pm 0.2$ pJ m^{-1}. Finally, we fit the field dependence of the transmission amplitude to an exponential decay $\Delta L_{21} \propto \exp(-D/L_{\text{att}})$ [Fig. 1(g)], for which we adopted the low wave-vector approximation of the attenuation length $L_{\text{att}} = v_g/2\pi\alpha f_{\text{res}}$, where f_{res} is derived from the Kalinikos-Slavin expression [32]. We obtain a Gilbert damping of $\alpha = 9.1 \pm 0.5\ 10^{-4}$, which appears slightly bigger than previously reported values on similar sputtered thin YIG films [25,34]. We note that the same methodology applied to the $D = 5$ μm straight antenna device gives very close results within the estimated error bars.

C. Comparison with near-field diffraction simulations

In order to assess the conformity of our measurements, we performed NFD simulations [27] for each field value for the straight and circular excitation antennas. Figures 2(a) and 2(b) show the simulated magnetization amplitude expressed in milliteslas for a YIG film magnetized out of the plane with an external field of $\mu_0 H_{\text{ext}} = 419.2$ mT and an excitation frequency of $f_{\text{exc}} = 6.892$ GHz for (a) a $(\pi/2)$ R-long straight CPW and (b) a quarter-circular CPW with radius of curvature $R = 10$ μm. Both CPWs have the same lateral dimensions, namely a central line $w_s = 400$ nm and a ground line $w_g = 200$ nm, as the measured devices. We defined the microwave magnetic field components (h_x, h_y) from the Oersted field of a straight conductor with rectangular section carrying uniform current density, whose value was adjusted according to typically used input power and impedance of the antennas. We note that the field distribution obtained with this somewhat crude approximation compares very well with finite-element simulations of curved CPWs [27].

In order to compare the simulations with propagating spin-wave spectra obtained from several pairs of antennas, we perform a sum over an effective area where the detection antenna is located as represented in white on the simulations in Figs. 2(a) and 2(b), and multiplied by the pixel area $dxdy$. Indeed, the coupling of a spin waves with a CPW, which is inductive in nature, can be estimated by the magnetic flux sensed by the antenna. Although it does not strictly correspond to the dynamic field radiated from the spin wave that the probe antenna senses, this rather simple averaging method provides a comprehensive estimate of the antenna's shape-dependent transduction, which we express in units of magnetic flux [e.g., in femtoWeber (fWb)]. Figure 2(c) summarizes the field dependence of all measured transmission amplitudes (ΔL_{21}, left y-axis) compared with the emulated inductive signal from the NFD simulations (right y-axis) for both the straight and concentric pairs of antennas. We find an excellent match between the amplitude of the measured transmission spectra and the simulated inductive signal over the whole field range for both the $D = 5$ μm and the $D = 8$ μm series. The agreement between measurements and simulations is all the better here for the antenna design matching the confined diffraction pattern (e.g., no spin-wave dynamics is to be found in the transition to the probe antenna's termination). This explanation of the differences in link budget between concentric and straight pairs of antennas validates our understanding of spin-wave transduction in curvilinear geometries in terms of NFD.

Furthermore, the amplitude ratio $(\Delta L_{21}^{\text{concentric}}/\Delta L_{21}^{\text{straight}})$ remains fairly constant and close to the square root of the radius ratio $\sqrt{R_2/R_1}$, namely $(\Delta L_{21}^{\text{concentric}}/\Delta L_{21}^{\text{straight}})_{5\,\mu m} \approx 0.66 \pm 0.01$ and $(\Delta L_{21}^{\text{concentric}}/\Delta L_{21}^{\text{straight}})_{8\,\mu m} \approx 0.43 \pm 0.01$. The comparison is better for the longer separation distance as suggested by the analogy with the Friis formula, which only applies in the far-field region.

III. YOUNG'S INTERFERENCE EXPERIMENT

Here we explore the idea of magnon beamforming from the shape of an excitation antenna, and propose to reiterate a Young's interference experiment with two seemingly circular apertures. Figures 3(a)–3(c) show SEM images of the Young's interference devices consisting in two adjacent semi-circular 1- μm wavelength CPW, having each a 1- μm curvature radius for the central line, and whose centers are 2 μm apart. We fabricated a series of 6six such devices on top of a 20-nm-thin $Ni_{80}Fe_{20}$ film, changing the location of the probe antenna, that is, keeping the same $x = 4$ μm and varying $y = \{0.0, 0.47, 0.9, 1.375, 2.0, 3.0\}$. In this manner, we can perform a discrete mapping of this Young's interference pattern with submicrometer resolution, using a 1-μm^2 square CPW as probe antenna. The tightness of the aimed curvature would not allow us to fabricate this submicrometer-size geometry on a YIG film, due to the limitations posed by the conductive resin [35].

Figure 3(d) shows the transmission spectra ΔL_{21} (colored lines, left y-axis) and reflection spectra ΔL_{11} (black line, right y-axis) for the three devices with a probe antenna position at $y = 0$ for the device shown in Fig. 3(a), $y = 0.9$ μm for that of Fig. 3(b), and $y = 2$ μm for that of Fig. 3(c). All devices were measured at −15 dBm input power, and for three different applied fields: 1.061 T, 1.134 T, and 1.212 T. The transmission spectra display a first peak at lower frequency, which should not be mistaken for a propagating spin wave signal, as it is aligned with the $k = 0$ peak of the reflection spectra (black line). Therefore, we focus on the remaining part of the spectra featuring the typical oscillations of the k_1 spin-wave mode, in order to track the change of amplitude with the probe antenna position. For the three field values, the oscillation amplitude appears maximum for the $y = 0$ device, it is significantly reduced for the $y = 0.9$ μm device, while it increases again for the $y = 2$ μm device.

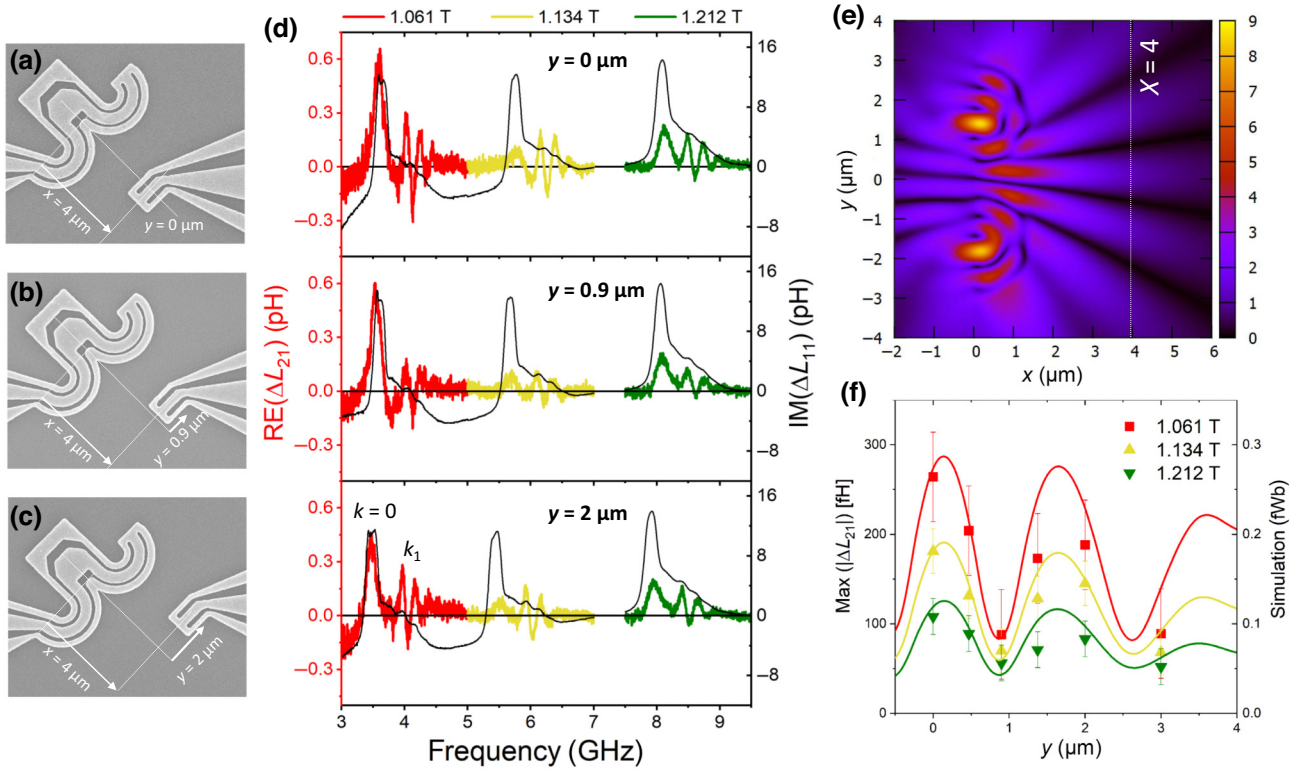

FIG. 3. (a)–(c) SEM images of three Young's interference devices with different location of probe antenna. (d) Transmission (left y-axis), and reflection spectra (black line, right y-axis) for the corresponding devices. (e) NFD simulation of a Young's interference antenna performed at $\mu_0 H_{ext} = 1.061$ T and $f = 4.07$ GHz. (f) Comparison of the evolution of the spin wave amplitude at $x = 4$ µm with the emulated inductive signal from the NFD simulations (color palette in unit of mT).

Figure 3(e) shows an NFD simulation of this Young's interference device done at $\mu_0 H_{ext} = 1.061$ T and $f = 4.07$ GHz, using the following set of parameters in accordance with prior characterization of this permalloy film [36]: a saturation magnetization of $\mu_0 M_s = 0.95$ T, a gyromagnetic ratio $\gamma = 29.8$ GHz T^{-1}, a Gilbert damping constant $\alpha = 7.5 \cdot 10^{-3}$, and exchange constant $A_{exch} = 7.5$ pJ m^{-1}. The diffraction pattern clearly shows the formation of spin-wave beams separated by dark zones, corresponding respectively to the constructive and destructive interference of spin waves in a similar fashion as a double-slit experiment in optics.

Finally, we compare in Fig. 3(f) the transmission spectra amplitude obtained on the six devices with the emulated inductive signal from the corresponding NFD simulations as described in Sec. II. We obtain a satisfying agreement, reproducing on the one hand the spatial dependence of the spin-wave diffraction pattern over two constructive interference beams, and on the other hand the comparative amplitude between the three field values. The small discrepancy between simulations and measurements could be due to the part of the CPW that transitions to the 1-µm^2 termination, which can slightly pick up some flux within the remaining diffraction pattern. In essence, this study demonstrates the possibility of shaping spin-wave beams from the shape of an antenna, and resolving the submicrometer featured size diffraction pattern with a 1-µm^2 inductive probe. While large-scale mappings of spin-wave diffraction from curved antennas have been achieved with either microfocused Brillouin light scatttering [37] or time resolved magneto-optical Kerr effect [38], the vector network analyzer-inductive probing scheme stands out for sensing submicrometer-wavelength diffraction patterns [21]. Furthermore, it is particularly suited to resolving efficiently both amplitude and phase information of the spin-wave propagation over a broad range of the microwave spectra, for which the acquisition time of a full two-ports spectrum is typically less than a minute. Nonetheless, our method requires fabricating several pair of antennas to obtain spatial information.

IV. CONCLUSION

We presented a study on the spin-wave transduction from curved excitation antennas, comparing transmission spectra with simulated mappings of the spin-wave amplitude for various geometries of excitation. We first showed that the difference in transmission amplitude between pairs of straight antenna versus concentric antennas was very well reproduced over a broad frequency range by an

emulated inductive signal built from the NFD mapping combined with the probe antenna definition. This validates our understanding of spin-wave transduction in curvilinear geometries in terms of NFD. Secondly, we reiterated a Young double-slit experiment with an antenna made of two adjacent semi-circular CPWs, acting like two seemingly circular apertures. We satisfactorily reproduced the simulated spin-wave diffraction pattern with a series of devices varying the position of probe antenna. We demonstrated in particular the possibility of inductively sensing the spin-wave amplitude with a 1-μm^2 spatial resolution. These results provide a methodology to explore the magnon beamforming through the shape of an excitation antenna, and pave the way for future development of interferometric magnonic sensors.

ACKNOWLEDGMENTS

The authors would also like to acknowledge the financial support of the French National Research Agency (ANR) under the MagFunc project, the Département du Finistère through the SOSMAG project, and also the Transatlantic Research Partnership, a program of the FACE Foundation and the French Embassy under the Magnon Interferometry project. We also acknowledge financial support by the Interdisciplinary Thematic Institute QMat, as part of the ITI 2021-2028 Program of the University of Strasbourg, CNRS and Inserm, IdEx Unistra (ANR 10 IDEX 0002), SFRI STRAT'US Project (ANR 20 SFRI 0012) and ANR-17-EURE-0024 under the framework of the French Investments for the Future Program.

[1] G. A. M. A. G. Gurevich, *Magnetization Oscillations and Waves* (CRC Press, Boca Raton, Florida, 1996).
[2] A. V. Chumak, A. A. Serga, and B. Hillebrands, Magnonic crystals for data processing, J. Phys. D: Appl. Phys. **50**, 244001 (2017).
[3] G. Csaba, Á. Papp, and W. Porod, Perspectives of using spin waves for computing and signal processing, Phys. Lett. A **381**, 1471 (2017).
[4] A. Barman, *et al.*, The 2021 magnonics roadmap, J. Phys.: Condens. Matter **33**, 413001 (2021).
[5] P. Pirro, V. I. Vasyuchka, A. A. Serga, and B. Hillebrands, Advances in coherent magnonics, Nat. Rev. Mater. **6**, 1114 (2021).
[6] A. V. Chumak, in *Spintronics Handbook: Spin Transport and Magnetism*, Chapter Magnon Spintronics: Fundamentals of Magnon-Based Computing, 2nd ed. (CRC Press, Boca Raton, FL, 2019), p. 247.
[7] A. V. Chumak, *et al.*, Advances in magnetics roadmap on spin-wave computing, IEEE Trans. Magn. **58**, 1 (2022).
[8] A. Mahmoud, F. Vanderveken, F. Ciubotaru, C. Adelmann, S. Hamdioui, and S. Cotofana, Spin wave based approximate computing, IEEE Trans. Emerg. Top. Comput. **10**, 1932 (2022).
[9] V. V. Kruglyak, S. O. Demokritov, and D. Grundler, Magnonics, J. Phys. D: Appl. Phys. **43**, 260301 (2010).
[10] J. Grollier, D. Querlioz, K. Y. Camsari, K. Everschor-Sitte, S. Fukami, and M. D. Stiles, Neuromorphic spintronics, Nat. Electron. **3**, 360 (2020).
[11] Á. Papp, W. Porod, and G. Csaba, Nanoscale neural network using non-linear spin-wave interference, Nat. Commun. **12**, 6422 (2021).
[12] A. Papp, G. Csaba, and W. Porod, Characterization of nonlinear spin-wave interference by reservoir-computing metrics, Appl. Phys. Lett. **119**, 112403 (2021).
[13] D. A. Allwood, M. O. A. Ellis, D. Griffin, T. J. Hayward, L. Manneschi, M. F. K. Musameh, S. O'Keefe, S. Stepney, C. Swindells, M. A. Trefzer, E. Vasilaki, G. Venkat, I. Vidamour, and C. Wringe, A perspective on physical reservoir computing with nanomagnetic devices, Appl. Phys. Lett. **122**, 040501 (2023).
[14] A. Khitun, Magnonic holographic devices for special type data processing, J. Appl. Phys. **113**, 164503 (2013).
[15] A. Khitun, Parallel database search and prime factorization with magnonic holographic memory devices, J. Appl. Phys. **118**, 243905 (2015).
[16] Á. Papp, W. Porod, Á. I. Csurgay, and G. Csaba, Nanoscale spectrum analyzer based on spin-wave interference, Sci. Rep. **7**, 9245 (2017).
[17] O. Gladii, M. Haidar, Y. Henry, M. Kostylev, and M. Bailleul, Frequency nonreciprocity of surface spin wave in permalloy thin films, Phys. Rev. B **93**, 054430 (2016).
[18] J. A. Otálora, M. Yan, H. Schultheiss, R. Hertel, and A. Kákay, Curvature-induced asymmetric spin-wave dispersion, Phys. Rev. Lett. **117**, 227203 (2016).
[19] M. Grassi, M. Geilen, D. Louis, M. Mohseni, T. Brächer, M. Hehn, D. Stoeffler, M. Bailleul, P. Pirro, and Y. Henry, Slow-wave-based nanomagnonic diode, Phys. Rev. Appl. **14**, 024047 (2020).
[20] C. Liu, *et al.*, Long-distance propagation of short-wavelength spin waves, Nat. Commun. **9**, 738 (2018).
[21] L. Temdie, V. Castel, C. Dubs, G. Pradhan, J. Solano, H. Majjad, R. Bernard, Y. Henry, M. Bailleul, and V. Vlaminck, High wave vector non-reciprocal spin wave beams, AIP Adv. **13**, 025207 (2023).
[22] L. Temdie, V. Castel, T. Reimann, M. Lindner, C. Dubs, G. Pradhan, J. Solano, R. Bernard, H. Majjad, Y. Henry, M. Bailleul, and V. Vlaminck, Chiral excitation of exchange spin waves using gold nanowire grating, Magnetochemistry **9**, 199 (2023).
[23] J. Stigloher, M. Decker, H. Körner, K. Tanabe, T. Moriyama, T. Taniguchi, H. Hata, M. Madami, G. Gubbiotti, K. Kobayashi, T. Ono, and C. Back, Snell's law for spin waves, Phys. Rev. Lett. **117**, 037204 (2016).
[24] P. Gruszecki, M. Mailyan, O. Gorobets, and M. Krawczyk, Goos-Hänchen shift of a spin-wave beam transmitted through anisotropic interface between two ferromagnets, Phys. Rev. B **95**, 014421 (2017).
[25] N. Loayza, M. B. Jungfleisch, A. Hoffmann, M. Bailleul, and V. Vlaminck, Fresnel diffraction of spin waves, Phys. Rev. B **98**, 144430 (2018).
[26] J. Gräfe, P. Gruszecki, M. Zelent, M. Decker, K. Keskinbora, M. Noske, P. Gawronski, H. Stoll, M. Weigand, M. Krawczyk, C. H. Back, E. J. Goering, and G. Schütz, Direct observation of spin-wave focusing by a Fresnel lens, Phys. Rev. B **102**, 024420 (2020).

[27] V. Vlaminck, L. Temdie, V. Castel, M. B. Jungfleisch, D. Stoeffler, Y. Henry, and M. Bailleul, Spin wave diffraction model for perpendicularly magnetized films, J. Appl. Phys. **133**, 053903 (2023).
[28] M. B. Jungfleisch, J. Ding, W. Zhang, W. Jiang, J. E. Pearson, V. Novosad, and A. Hoffmann, Insulating nanomagnets driven by spin torque, Nano Lett. **17**, 8 (2016).
[29] M. Bailleul, D. Olligs, and C. Fermon, Propagating spin wave spectroscopy in a permalloy film: A quantitative analysis, Appl. Phys. Lett. **83**, 972 (2003).
[30] V. Vlaminck and M. Bailleul, Spin-wave transduction at the submicrometer scale: Experiment and modeling, Phys. Rev. B **81**, 014425 (2010).
[31] H. Friis, A note on a simple transmission formula, Proc. IRE **34**, 254 (1946).
[32] B. A. Kalinikos, Spectrum and linear excitation of spin waves in ferromagnetic films, Sov. Phys. J. **24**, 718 (1981).
[33] B. A. Kalinikos and A. N. Slavin, Theory of dipole-exchange spin wave spectrum for ferromagnetic films with mixed exchange boundary conditions, J. Phys. C: Solid State Phys. **19**, 7013 (1986).
[34] S. Li, W. Zhang, J. Ding, J. E. Pearson, V. Novosad, and A. Hoffmann, Epitaxial patterning of nanometer-thick $Y_3Fe_5O_{12}$ films with low magnetic damping, Nanoscale **8**, 388 (2016).
[35] Protective coating AR-PC 5091.02 (Electra 92). https://www.allresist.com/portfolio-item/protective-coating-ar-pc-5091-02-electra-92/.
[36] V. Vlaminck, Décalage Doppler d'ondes de spin induit par un courant électrique. PhD dissertation, University of Strasbourg, IPCMS (2008), a full PhD Thesis entry, https://www.theses.fr/2008STR13128.
[37] M. Madami, Y. Khivintsev, G. Gubbiotti, G. Dudko, A. Kozhevnikov, V. Sakharov, A. Stal'makhov, A. Khitun, and Y. Filimonov, Nonreciprocity of backward volume spin wave beams excited by the curved focusing transducer, Appl. Phys. Lett. **113**, 152403 (2018).
[38] Á. Papp, M. Kiechle, S. Mendisch, V. Ahrens, L. Sahin, L. Seitner, W. Porod, G. Csaba, and M. Becherer, Experimental demonstration of a concave grating for spin waves in the Rowland arrangement, Sci. Rep. **11**, 14239 (2021).

Correction: The previously published order of authors was presented incorrectly and has been fixed.